Structural transformations and disordering in zirconolite ($CaZrTi_2O_7$) at high pressure

Ashkan Salamat,[a]* Paul F. McMillan,[b]* Steven Firth,[b] Katherine Woodhead,[b] Andrew L. Hector,[c] Gaston Garbarino,[a] Martin C. Stennett[d] and Neil C. Hyatt[d]

[a] European Synchrotron Radiation Facility, BP 220, 38043 Grenoble, Cedex 9, France. ashkan.salamat@esrf.fr

[b] Department of Chemistry, University College London, London WC1H 0AJ, UK. p.f.mcmillan@ucl.ac.uk

[c] Chemistry, University of Southampton, Southampton SO17 1BJ, UK

[d] Department of Materials Science & Engineering, The University of Sheffield, Mappin Street, Sheffield, S1 3JD, UK

Abstract: There is interest in identifying novel materials for use in radioactive waste applications and studying their behavior under high pressure conditions. The mineral zirconolite ($CaZrTi_2O_7$) exists naturally in trace amounts in diamond-bearing deep-seated metamorphic/igneous environments, and it is also identified as a potential ceramic phase for radionuclide sequestration. However, it has been shown to undergo radiation-induced metamictization resulting in amorphous forms. In this study we probed the high pressure structural properties of this pyrochlore-like structure to study its phase transformations and possible amorphization behavior. Combined synchrotron X-ray diffraction and Raman spectroscopy studies reveal a series of high pressure phase transformations. Starting from the ambient pressure monoclinic structure an intermediate phase with $P2_1/m$ symmetry is produced above 15.6 GPa *via* a first order transformation resulting in a wide coexistence range. Upon compression to above 56 GPa a disordered metastable phase III with a cotunnite-related structure appears that is recoverable to ambient conditions. We examine the similarity between the zirconolite behavior and the structural evolution of analogous pyrochlore systems under pressure.

Introduction

Zirconolite is found as an accessory mineral in deep-seated volcanic rocks including kimberlites and carbonatites that can be diamond-bearing, and as a detrital phase following weathering. It is also proposed as a main component of the synthetic rock assemblage SYNROC designed to immobilise large actinide ions derived from high level radioactive waste products that can be incorporated within the refractory ceramic structure.[1, 2]

The zirconolite structure can be considered as a derivative of the $A_2B_2O_7$ pyrochlore structure, where A and B represent large 8-coordinate and small 6-coordinate cations, respectively (Figure 1).[3-7] The zirconolite and pyrochlore structures share a common hexagonal tungsten bronze (HTB) motif, forming (111) planes in the cubic (*Fd*-3*m*) pyrochlore structure. Compression along the [111]

direction of the pyrochlore structure results in the monoclinic (*C*2/*c*) zirconolite-2M structure, in which the HTB layers lie perpendicular to the [001] direction.[3-7] Writing the general zirconolite structure as ABC_2O_7, the HTB layers comprise two octahedral sites (C1 and C3) forming six membered rings, within which are located five- coordinate (C2) sites that are 50% occupied; the A and B cation sites are 8- and 7-coordinate, respectively, and form an ordered array between the HTB layers.[3-7] Various zirconolite polytypes with complex superstructures have been described depending upon the cation site occupancy, vacancy distribution and relative displacement of HTB layers.[3-7]

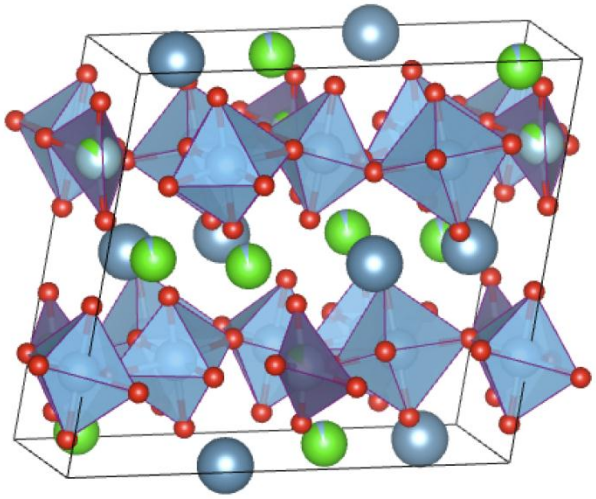

Figure 1. Structural model of the starting ambient phase of $CaZrTi_2O_7$ (*C*2/*c*). Colour code: Ca atoms, large and in dark grey, Zr atoms and ZrO_7 polyhedra in green, Ti atoms and TiO_6 polyhedra in light grey, $Ti(Zr)O_4$ tetrahedra in purple.

In the context of radioactive waste applications, natural specimens of zirconolite have been demonstrated to retain their actinide inventory and they show very limited evidence of alteration over geological time scales.[8, 9] Synthetic analogues of natural zirconolite, based on the formula $CaZrTi_2O_7$, target substitution of trivalent and tetravalent actinides and lanthanide fission products on the Ca and Zr sites based on the comparable ionic radii of these species, with charge compensation introduced on the Ti site as necessary.[10-15]

Actinide species incorporated within host crystalline lattices undergo alpha decay processes resulting in substantial structural damage that may eventually result in a radiation amorphized or "metamict" material as reviewed by Weber *et al*.[16] For example, α-decay of Pu-239 affords an energetic (5.2 MeV) α-particle and a U-235 daughter which recoils with an energy of 86 keV. The □-particle deposits its energy in ionisation processes causing relatively few atomic displacements, but recoil of the daughter atom produces 10^3 atomic displacements through ballistic collisions, within a 10^2 nm cascade.[16] Defect accumulation and cascade overlap eventually result in amorphization of the initially crystalline host material. In the case of zirconolites the radiation amorphized structure appears to be stabilized by formation of TiO_5 polyhedra at the expense of the TiO_6 polyhedra initially present.[17, 18] Many experimental and simulation studies have been carried out to investigate the nature of the disordering process and the properties of the metamict materials.[16] It is useful to compare the results with the properties and formation mechanisms of amorphous materials produced by other methods. Usually glass formation involves quenching from a high temperature

liquid state. Another method involves pressure-induced amorphization (PIA), where static or dynamic high pressures are applied to cause structural disordering within crystalline solids.[19-21]

The present study was initiated to investigate the possibility of PIA occurring among synthetic zirconolite samples. Initial results obtained by Raman spectroscopy in a diamond anvil cell indicated an irreversible disordering process occurring above P~30 GPa. However, subsequent X-ray diffraction (XRD) studies showed that the disordering process was associated with a kinetically impeded crystal-crystal phase transformation. We have recently observed a similar effect during compression of $Bi_2Ti_2O_7$ and $Bi_2Sn_2O_7$ pyrochlore materials in which metastable defective fluorite-related structures were obtained at high pressure.[22] This study reveals new relationships between zirconolite, pyrochlore, fluorite and perovskite-related structure types that can be encountered during metastable pressurization and radiation-induced metamictization processes.

Experimental

Zirconolite samples ($CaZrTi_2O_7$) were prepared by ball milling a stoichiometric mixture of the component oxides CaO, ZrO_2 and TiO_2, then pressing into a pellet and sintering at 1450 °C for 8 hours. XRD and Raman investigations indicated that a pure phase of $CaZrTi_2O_7$ (*C*2/*c*) was obtained. Additional fluorescence lines were recorded during our initial Raman studies using 785 nm laser radiation; these are due to low levels of rare earth ions (mainly Nd^{3+}) incorporated as ppm level impurities within the starting materials. Selected area electron diffraction (SAED) patterns of $CaZrTi_2O_7$ were obtained, down specific crystallographic zone axes, using a Philips EM 420 transmission electron microscope (TEM), operating at 120 keV. SAED patterns were acquired from a number of different grains and the composition of all the grains were confirmed to be consistent with the proposed stoichiometry by qualitative energy dispersive spectroscopy (EDX). The sample was prepared for TEM by conventional mechanical thinning, followed by ion beam milling using a Gatan Precision Ion Polishing System (PIPS) to achieve electron transparency. For high pressure measurements powdered samples were placed inside membrane driven cylindrical diamond anvil cells (DACs) using 200 or 300 μm culet diamonds. Rhenium gaskets were laser drilled to provide the sample chamber. A ruby chip was placed alongside the sample to act as a pressure calibrant.[23] The Raman and laser-excited fluorescence spectroscopy was carried out using home-built[24] and Renishaw optical systems. For optical spectroscopy studies samples were loaded into DACs using cryogenic techniques with N_2 as a pressure-transmitting medium (PTM). There is no or minimal contribution from the N_2 PTM in our optical studies in the region of interest. During initial X-ray experiments samples were loaded without any PTM present in order to promote highly non-hydrostatic conditions and thus engage the presumed onset of PIA. However, we later recognized that disordered crystalline phase transitions were occurring instead of PIA, and further experiments were carried out using a He PTM to determine the equation of state and examine the compression behavior under near-hydrostatic conditions. Synchrotron angle dispersive X-ray diffraction studies were carried out at high pressure beamlines ID27 (European Synchrotron Radiation Facility, France, λ= 0.3738 Å) and I15 (Diamond Light Source, UK, λ= 0.4421 Å). Diffraction patterns were recorded as 2-D angle-dispersive data sets using a MAR image plate or CCD detectors and analyzed using Fit2D and EXGUI GSAS software packages.[25-27]

Results

Electron diffraction results for starting materials

The ABC_2O_7 zirconolite structure exhibits a wide range of polytypes constructed from two HTB layers with an intervening layer of A and B cations.[3-7] Intergrowth defects are also commonly observed giving rise to variation in the stacking relationship between adjacent structural modules. The occurrence of polytypes and intergrowth defects thus depends sensitively on the chemical composition, and even a small concentration of dopant species (particularly rare earth cations) may be sufficient to result in complex intergrowth defects that are not readily detectable using X-ray powder diffraction techniques. However, such intergrowth defects are readily evidenced in zone axis electron diffraction patterns by characteristic streaking associated with structural disorder in the corresponding real space direction. The zirconolite samples studied here incorporated adventitious Nd^{3+} species, at low (ppm level) concentration, as evidenced by the initial Raman/luminescence studies. It was considered appropriate to confirm the presence or absence of such intergrowth defects, to evaluate their possible influence on the phase transformation behavior during compression. The zone axis electron diffraction patterns shown in Figure 2 were indexed in the *C*2/*c* space group for the zirconolite-2M structure reported by Gatehouse *et al*.[3] No evidence of streaking was apparent, demonstrating the absence of significant intergrowth defects. This observation shows that we can ignore the presence of minor impurities on the compression results.

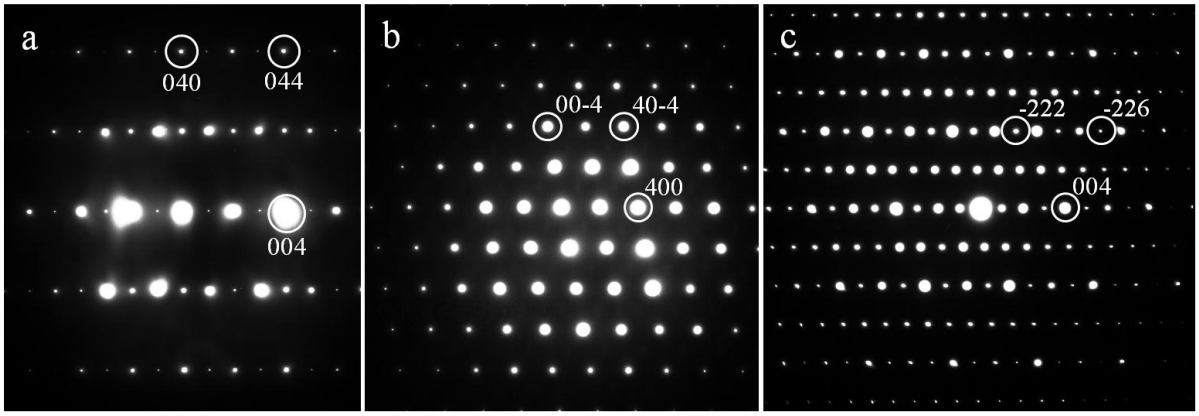

Figure 2. Zone axis electron diffraction patterns, indexed in the *C*2/*c* space group for the zirconolite-2M structure[3] (a) [100], (b) [010], and (c) [110] zone axes.

Raman and fluorescence spectroscopy results

The starting zirconolite sample was examined using 514.5 and 785nm laser excitation. The 514.5 nm spectrum showed only the main phonon peaks below 800 cm^{-1} (Figure 3), with additional weak features near 1500 and 3200 cm^{-1}. These were readily identified as electronic transitions occurring among the 4f sublevels of trace amounts of Nd^{3+} incorporated adventitiously within the sample: 785 nm laser excitation showed additional strong Nd^{3+} fluorescence peaks appearing near 1500 cm^{-1}. These are due to the $^4F_{3/2}$-$^4I_{9/2}$ transition following excitation into the $^4F_{3/2}$ manifold. Laser excited fluorescence techniques could provide a powerful method for studying the local site symmetry of rare earth or actinide ions incorporated within ceramic structures. However, this technique could not be applied in our high pressure studies because of overlap between the luminescence signal and first order Raman scattering from the diamond windows.

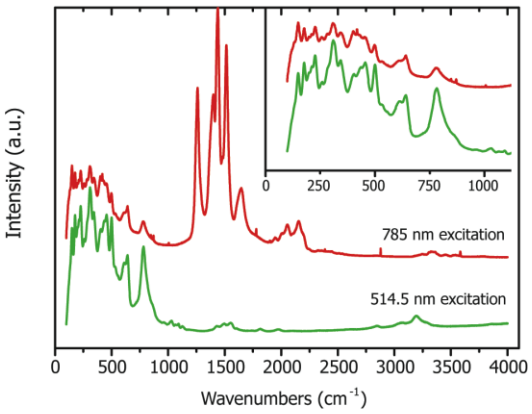

Figure 3. Vibrational Raman and electronic fluorescence spectra collected at ambient conditions for $CaZrTi_2O_7$ zirconolite samples using 785 nm and 514 nm laser excitation. The strong peaks observed above 1000 cm^{-1} with the red laser line are due to electronic transitions of a rare earth cation (likely Nd^{3+}) present as a trace impurity within the sample. The inset shows the vibrational Raman spectra obtained with both laser excitations.

The ambient pressure Raman spectrum exhibits a main peak at 780 cm^{-1} due to symmetric stretching of TiO_6 groups. The intensity of this peak is significantly greater using the green (514.5 nm) laser excitation indicating a possible resonance enhancement and as the highest frequency vibration observed and must be due to stretching of the lightest ion (O_2-) against the metal (Ti) to which it is strongly bound. This peak is present up to 41 GPa (Figure 4). Below 700 cm^{-1} other TiO_6 stretching and bending vibrations occur as well as modes associated with the ZrO_7 and CaO_8 polyhedral vibrations.

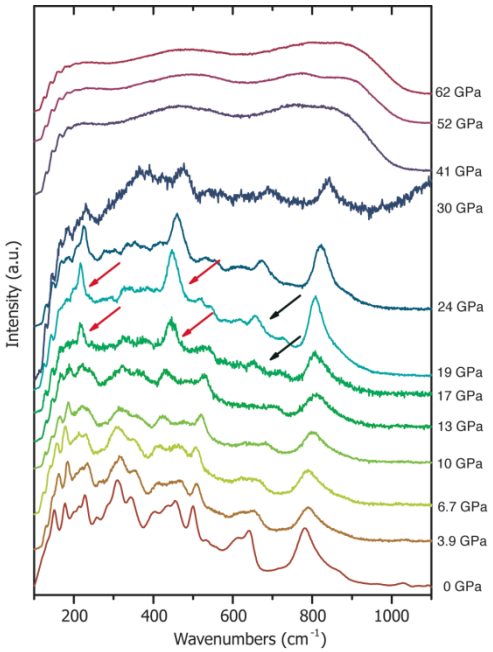

Figure 4. The Raman spectra of zirconolite during compression at ambient temperature in N_2 pressure transmitting medium obtained using 514.5 nm laser radiation. The full spectral compression data up to a final pressure of 62 GPa are shown with selected patterns highlighting the appearance of new Raman peaks associated with the onset of a phase transition.

As the pressure is increased, the peaks in the 150-550 cm^{-1} region became broadened but all the features of the low pressure zirconolite phase could still be identified up to P ~ 13 GPa (Figure 4). Above this pressure a new feature appears around 650 cm^{-1} (as indicated by the black arrow in Figure 4) and the spectrum is dominated by three strong bands near 800, 450 and 220 cm^{-1} (two of which are indicated by the red arrows in Figure 4). The appearance of these new modes and the intensity variations are associated with a phase transition identified by X-ray diffraction. In the 30 GPa spectrum these three features are diminished in intensity and a broad feature appears at ~350 cm^{-1}.

By 41 GPa all of the crystalline peaks have been lost and the spectrum contains only broad bands (Figure 4) Such behavior is often used to indicate the occurrence of PIA, in which the crystal structure has collapsed under extreme pressurization.[20, 28] The broad features are preserved upon decompression to ambient conditions (Figure 5). The broad band profile changes slightly during decompression, with a doublet emerging from within the high frequency band (600-800 cm^{-1}), and enhanced intensity observed in the lower wavenumber region (<400 cm^{-1}) (Figure 5). That could suggest some structural changes occurring within the "amorphous" material, which have been linked to the phenomenon of "polyamorphism" in previous studies.[20, 29, 30]

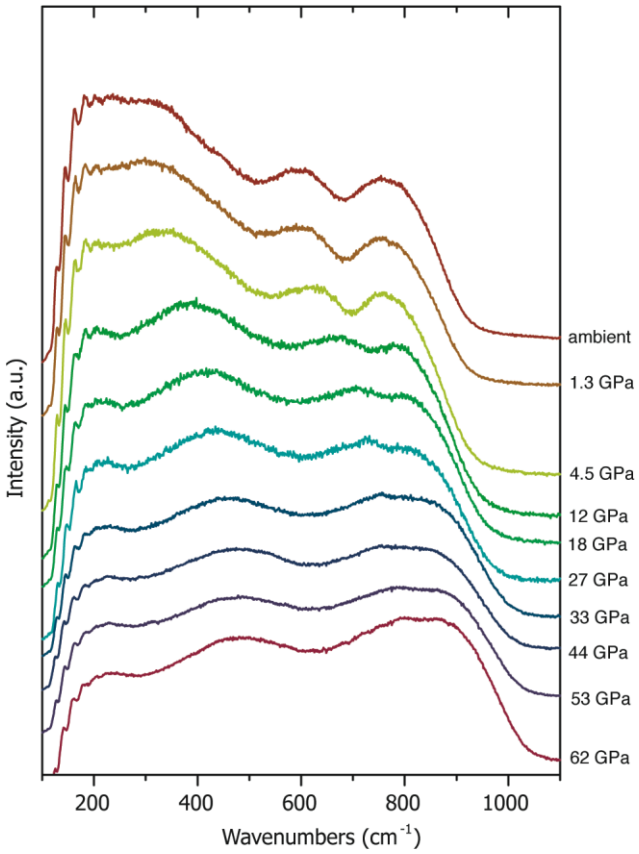

Figure 5. The Raman spectra of zirconolite during decompression at ambient temperature in N_2 pressure transmitting medium obtained using 514.5 nm laser radiation.

However, apart from the possible occurrence of PIA, other interpretations of the Raman data can be advanced. It is well known that crystalline materials with ordered atomic arrangements but

extensive vacancies can exhibit extreme broadening in their Raman and IR spectra, due to disruption of the phonon propagation relations, to result in observation of a vibrational density of states (VDOS) pattern: such effects have been described well for TiN_{1-x} materials.[31-33] Ti-bearing oxides including perovskites such as $BaTiO_3$ and $SrTiO_3$ can exhibit electron-phonon coupling and second order Raman scattering effects that can also result in broadening of spectral lines.[34, 35] A similar broadening was observed in the Raman spectra of $Bi_2Hf_2O_7$ on heating as it underwent phase changes from a pyrochlore-based structure with ordered bismuth displacements, to one in which bismuth atoms are statistically distributed across a number of sites within a crystallographically more symmetrical unit cell. The Raman spectral changes were observed to be correlated with structural phase transformations recorded by X-ray diffraction.[36]

Synchrotron X-ray diffraction studies

Compressibility of the C2/c zirconolite phase.

The unit cell parameters were refined using a Le Bail approach assuming the monoclinic structure was maintained until ~15 GPa. The cell parameters undergo little variation upon initial compression until above P ~3 GPa. The monoclinic angle remains approximately constant throughout the pressure range up to ~14 GPa. The main compression occurs along the *a* axis, which becomes reduced by approximately 3% over this pressure range (Figure 6).

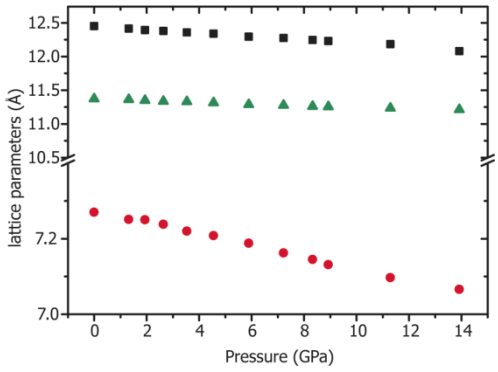

Figure 6. A plot of the lattice parameters of $CaZrTi_2O_7$ (*C2/c*) as a function of pressure up to 14 GPa. The black square, red circle and green triangle are representative of the a, b and c lattice parameters respectively. The values have been determined using Le Bail refinement.

Using the *C2/c* structure the V(P) relations were analyzed using a third order Birch-Murnaghan equation of state (Figure 7 (left)),[37, 38] as defined by:

$$P(V) = 3K_0 f(1+2f)^{5/2}\left(1+\frac{3}{2}(K_0'-4)f\right) \quad (1)$$

to obtain values for the bulk modulus (K_0) and its pressure derivative (K_0'), as well as to examine details up to the polymorphic transformations at higher pressure. K_0 and K' were then subsequently refined using a linearized version of the Birch-Murnaghan relation using finite strain (f) and normalized pressure (F) variables. The volume strain is expressed by:

$$f = \frac{1}{2}\left[\left(\frac{V_o}{V}\right)^{\frac{2}{3}} - 1\right] \quad (2)$$

and the normalized pressure F by:

$$F = P(3f(1+2f)^{5/2})^{-1} \quad (3)$$

This linearized extrapolation using a finite-strain equation permits the value of the y-axis intercept and the gradient of the fit to determine K_0 and K_0' respectively (Figure 7 (right)).[39, 40] A gradient of zero for the linear fit describes a value of $K_0' = 4$ and constrains the Birch-Murnaghan EOS to a third order.[41] The values obtained were K_0 = 188(15) GPa and $K_0' = 3.6(1)$ for initial compression of the *C2/c* zirconolite phase. These are comparable with the compressibility properties of related structures of $Bi_2Ti_2O_7$ (K_0 = 202 GPa; $K_0' = 2.9$)[22] and $Sm_2Ti_2O_7$ (K_0 = 164 GPa; $K_0' = 4$).[42]

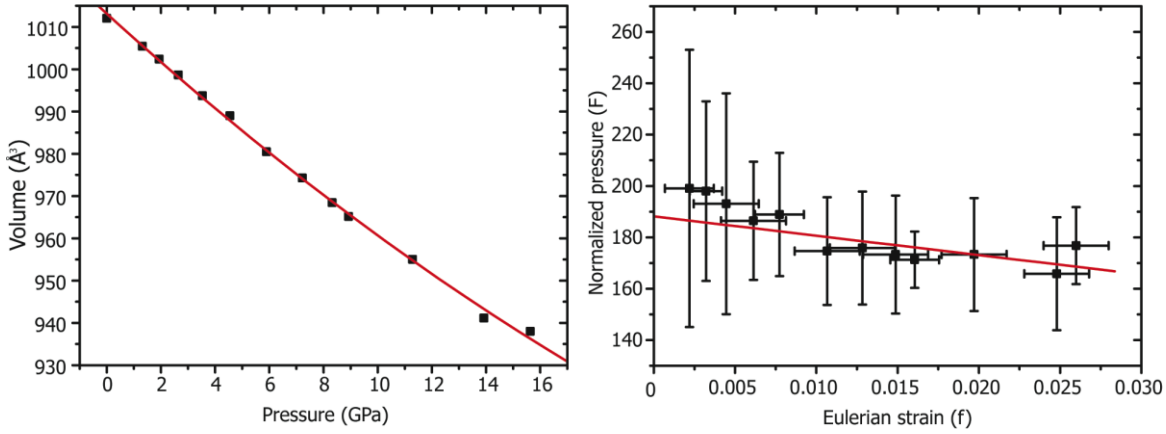

Figure 7. (left) A V(P) plot for the *C*2/*c* phase of $CaZrTi_2O_7$ up to P ~ 15 GPa. Data were fitted using a third order Birch Murnaghan equation of state. (right) The compressibility are further refined using a reduced variable normalized pressure (F) vs. Eulerian strain (f) providing compressibility values of K_0 = 188(15) GPa; $K_0' = 3.6(1)$

C2/c → P 2_1/m phase transition at 15-16 GPa

Samples studied under both hydrostatic and non-hydrostatic conditions exhibited a structural transformation into a new high density phase at high pressure (*C*2/*c* → *P*2_1/*m*). This is most clearly observed to occur at P = 15.6 GPa using He as a highly hydrostatic PTM surrounding the polycrystalline sample (Figure 8). The structural transformation is associated with a large hysteresis during recovery experiments, and persistence of the metastable co-existing structures was recorded up to 35 GPa during compression, indicating the presence of a first order transition into a new phase that we term zirconolite-II for convenience. During further compression the *P*2_1/m phase remained stable until 57 GPa (Figure 9).

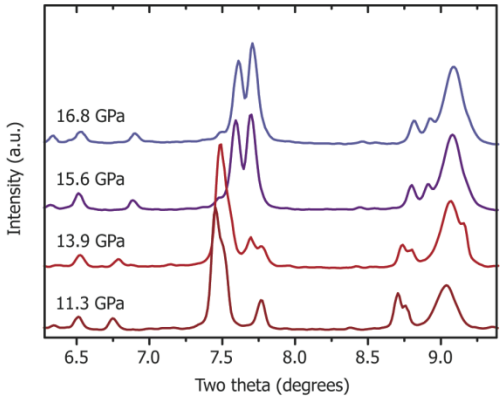

Figure 8. XRD diffraction collected at ESRF ID27 (λ = 0.3738 Å) for zirconolite ($CaZrTi_2O_7$) at high pressure in a DAC using a He as a pressure transmitting medium. A clear change in the diffraction pattern is observed between 13.9 and 15.6 GPa indicating transformation into a high-pressure phase (zirconolite-II).

Due to the prolonged co-existence range of the two phases, initial indexing of the X-ray diffraction data was carried out at 40 GPa during pressurisation, to ensure that no remnants of the low pressure pattern were present. All assigned peaks were fitted individually to provide an indexed solution. Several different unit cell shapes were generated using tetragonal to orthorhombic structures although close inspection of the diffraction data revealed some small additional peaks that indicated a lowered symmetry. The higher symmetry cells also had large cell volumes that would have to be described using a supercell solution. Structure solutions with a high figure of merit were obtained using monoclinic cells. The best Le Bail fit to the data used a monoclinic cell that described all observed peak positions, with lattice parameters of a=9.626(4) Å, b=6.672(3) Å, c=8.855(3) Å and β=102.8(2)° (wR_p = 6.7 % and R_p = 5.0 %.) at 40 GPa (Figure 10). Only two space groups ($P2_1$, $P2_1/m$) could satisfy the observed pattern of systematic absences (0k0: k = 2n).[43] We chose to use the higher symmetry description within space group $P2_1/m$. One complication in using data from this phase arose from the presence of overlapping Re diffraction contributions from the DAC gasket: these were excluded from the indexing and refinement procedure. This however led to further complication when attempting to elucidate a complete structure solution of the new phase from Rietveld analysis. A full structural search was conducted attempting to identify other systems with similar stoichiometry and unit cell shape and symmetry. However, this was infeasible from the quality of the high pressure data due to limited data range, uncertainties in the intensities and strong overlap with the gasket. Another problem was that because of the long pressure range of co-existence from ~15 GPa to ~35 GPa the indexing approach for identifying the crystal shape was carried out at the higher end of this pressure range. This introduces additional peak broadening and issues of deviatoric stress, even in a He PTM, making peak fitting more difficult and uncertain.

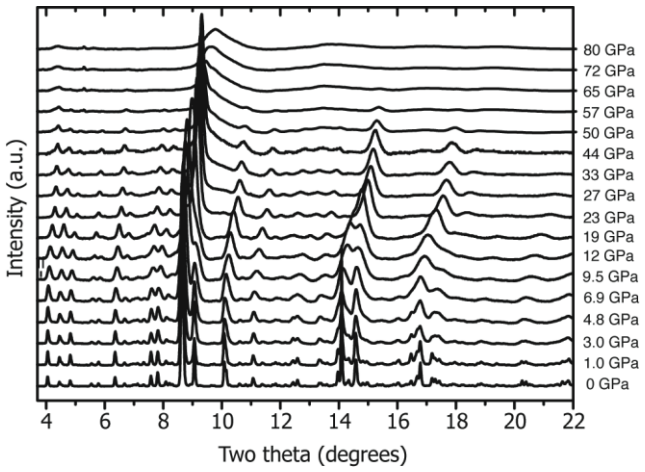

Figure 9. Angle dispersive X-ray diffraction data of $CaZrTi_2O_7$ up to a pressure of 80 GPa without any pressure transmitting medium present in the cell. These data were collected at DLS I15 (λ= 0.4421 Å).

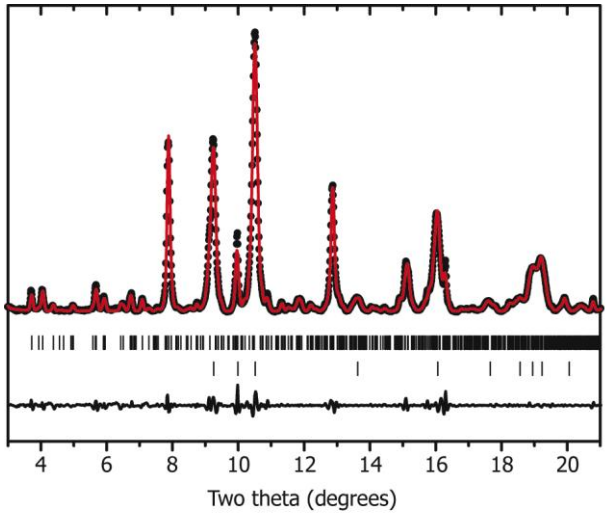

Figure 10. A Le Bail refinement carried out at 40 GPa of the high pressure phase of zirconolite-II ($CaZrTi_2O_7$). The unit cell is defined as monoclinic with a, b, c as 9.626(4) Å, 6.672(3) Å, 8.855(3) Å respectively and β as 102.8(2)°. There are two indistinguishable space groups that fulfill the reflection conditions (0k0: k = 2n) ie. systematic absences; $P2_1$ and $P2_1/m$. Data points and Le Bail fit are presented in black and red respectively. The upper set of tick marks are the allowed reflection positions and the lower set the reflection positions of rhenium from the DAC gasket.

Formation of a disordered phase at higher pressure and its recovery to ambient pressure

At above P ~41 GPa we observed dramatic changes occurring in the Raman spectrum with loss of identifiable crystalline features that were replaced by broad bands indicative of an amorphous or highly disordered crystalline material. We initially interpreted this result as indicating the potential occurrence of PIA within the zirconolite material, and that prompted our further series of X-ray diffraction measurements. The XRD studies then showed that the crystalline peaks associated with the monoclinic structure (zirconolite-II) were maintained up to 57 GPa, although some broadening appeared at the base of the principal reflection that emerges as a shoulder near 9.5° 2θ above ~33

GPa, and the diffraction lines show a loss in resolution during compression to P ~50 GPa (Figure 9). The diffraction spacings shift rapidly throughout this pressure range.

Different crystal structure solutions were then investigated to model the new high density zirconolite-III phase following the transformation, that was initiated at pressures perhaps as low as 30-40 GPa, from the comparison of X-ray and Raman results under different pressurization conditions. This phase transformation was only completed above approximately 70 GPa. The new polymorph could be recovered to ambient conditions, and all structural modeling was carried out using the diffraction data obtained from the decompressed sample (Figure 11).

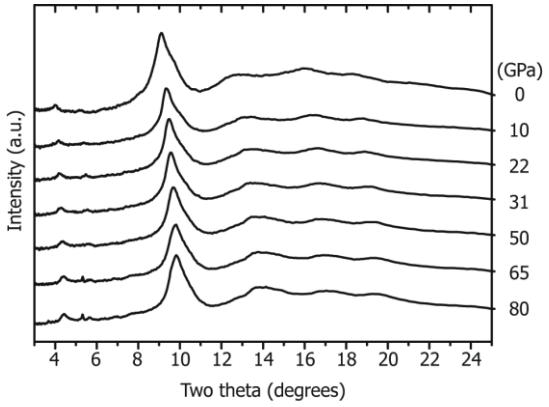

Figure 11. A stacked plot of XRD data obtained during decompression from 80 GPa. The high pressure zirconolite-II phase identified from analysis of the diffraction data at 40 GPa has fully transformed into a further polymorph with a distorted cubic structure (zirconolite-III) by around 70 GPa. These data show that this phase is recoverable to ambient conditions.

The first structural solution model attempted was that of a face centered cubic lattice (Figure 12 (a)) with a fluorite-like unit cell. Such a model has provided a good solution following compression/decompression studies of related pyrochlore structured materials.[22] However, although this model does provide a reasonable initial fit, it does not accurately describe all of the Bragg peaks, and especially the shoulder at ~ 10° along with the smaller feature at 10.5°. The good agreement with the data does suggest that the structure is fluorite-related with an overall symmetry close to cubic. The cell was then allowed to undergo a rhombohedral distortion, and the data refined to obtain an *R*-3*m* cell with a= 5.6 Å and α = 94.82° (Figure 12 (b)).

Another possible transformation that has been observed during pressurization of pyrochlore phases is into a defective perovskite structure.[44] The peak positions observed for zirconolite-III are close to those of a perovskite-type unit cell with a_o = 3.9 Å (Figure 12(c)). A slight rhombohedral distortion (α~92.5°) also permits a reasonable fit throughout the full pressure range but the fitting statistics were less good than those found for the rhombohedrally distorted fluorite-like solution.

Our final model was based on the orthorhombic cotunnite structure (*Pnma*) adopted by materials such as $PbCl_2$ and proposed by Zhang *et al.* as the partially disordered phase formed on pressurization of the pyrochlore $La_2Zr_2O_7$.[45] The dioxides UO_2, ThO_2, ZrO_2 and HfO_2 undergo a transition into the cotunnite structure at high pressure, and Li_2O transforms to an anti-cottunite structure. [46-48] Analysis of our results for zirconolite-III using a *Pnma* cell with a = 5.357(5) Å, b = 3.128(1) Å and c = 6.372(9) Å provides an excellent fit to the diffraction data, and a full Reitveld

refinement using this structure model also led to a good fit (Figure 12 (d)). The Ca, Zr and Ti atoms were placed on cation sites using statistically averaged positions to result in ¼ (Ca), ¼ (Zr) and ½ (Ti) site occupancies, and the atomic coordinates and U_{iso} parameters were constrained to remain constant throughout the refinement. The O^{2-} ions were placed on the anion sites along with an averaged vacancy concentration to achieve the A_4O_7 stoichiometry. The volume-pressure relationship and compressibility values for all four structural models are given in Figure 13.

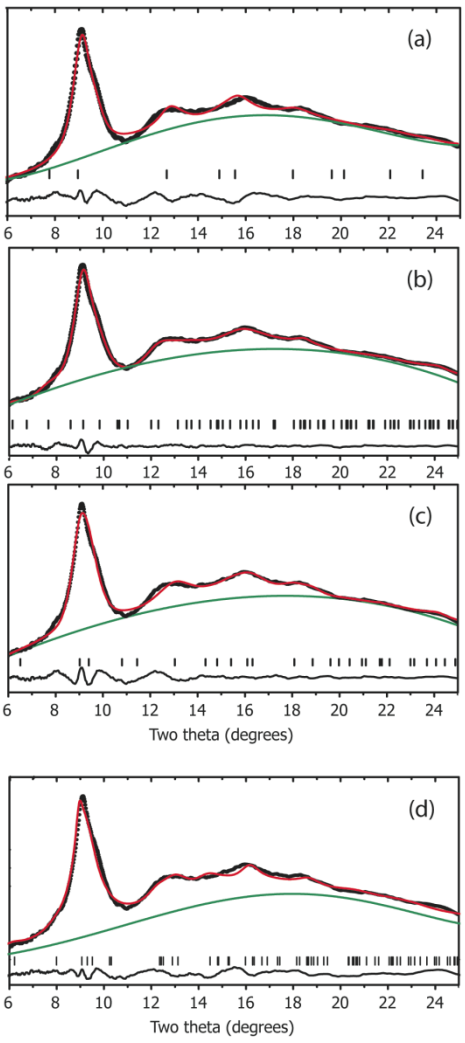

Figure 12. Structural refinement of the recovered zirconolite sample at ambient conditions following its subsequent decompression from 80 GPa. The data points, fits and background are represented in black, red and green respectively. λ = 0.442 Å (a) Le Bail fit using the *Fm*-3*m* space group with a = 5.52(2) Å. R_p = 0.55% and wR_p= 0.9%. (b) Le Bail fit using the *R*-3*m* space group with a = 5.52(2) Å and α = 94.82. R_p = 0.32% and wR_p= 0.53%. (c) Le Bail fit using the *R*-3*m* space group with a = 3.98(3) Å and α = 92.52(1) degrees R_p = 0.71% and wR_p= 1.0%. (d) Rietveld fit using the *Pnma* cotunnite structure with a = 5.357(5) Å, b = 3.128(1) Å and c = 6.372(9) Å. R_p = 0.87% and wR_p= 0.74%.

Despite the good observed fit to the X-ray data we cannot conclude that this represents a final structure solution to the data, because the diffraction features are too broad and it is impossible to obtain a statistically significant solution. In their related work on pyrochlore-derived systems, Zhang *et al.* noted that '... due to very broad peak width, it is impossible to resolve the structure…'.[45]

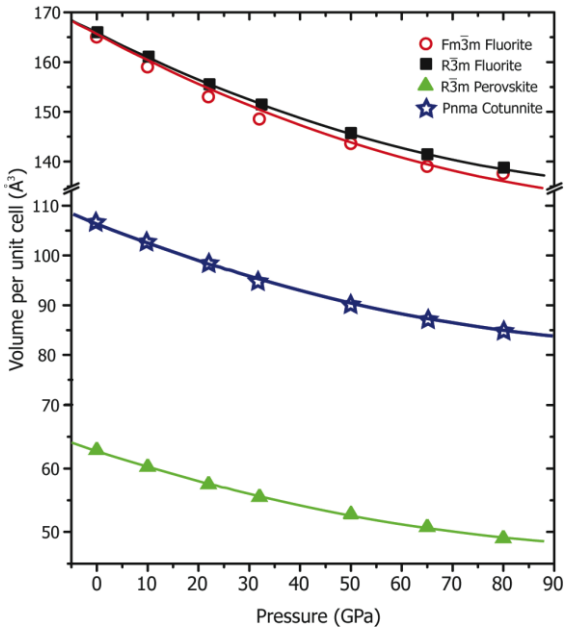

Figure 13. V(P) relations for the decompression of the high pressure phase of $CaZrTi_2O_7$ (zirconolite-III) analyzed using four different structural models. The bulk modulus values for the four models are as follows: (1) *Fm*-3*m* fluorite – K_0 = 225(19) GPa, K_0' = 6.8(0.9). (2) *R*-3*m* fluorite – K_0 = 282(12) GPa, K_0' = 4.7(0.2). (3) *R*-3*m* perovskites – K_0 = 208(12) GPa, K_0' = 3.5(0.2). (4) *Pnma* cotunnite – K_0 = 239(19) GPa, K_0' = 5.1(0.6)

Discussion

Several studies have reported that $A_2B_2O_7$ systems such as $Sm_2Ti_2O_7$, $Gd_2Ti_2O_7$ and other related materials become amorphous under pressurization at room temperature conditions. [49, 50] These conclusions were based on Raman spectroscopic studies that exhibited an irreversible loss of crystalline peaks that were replaced by broad phonon features that were recovered to ambient pressure.[42] The results were interpreted to suggest that at pressures between 40-50 GPa a mixture of amorphous and distorted pyrochlore structures was present associated with disordering on the anion site. Based on our current findings the same conclusions could be made from just our Raman study where we also observe the disappearance of any distinct Raman modes and the notion of amorphisation could be implied. However, it is evident from our XRD studies that the system has undergone significant disordering in its high pressure form but is not amorphous. Unlike the titanate pyrochlores of Sm and Gd the system maintains its disordered crystalline structure to quenched conditions.

The loss of features in both the Raman and XRD studies are due to the disordering in the anion sites that allow the TiO_6 octahedra to orientate randomly. There must be some inherent cation ordering that still gives rise to the dominant 211 reflections in the ambient phase and then in the high pressure structure above 15.6 GPa and present until above 60 GPa. However, we do not believe that the system is amorphous but rather that there is a metastable phase with some residual ordering (or an assemblage of co-existing structures derived from the same basic sub-cell) present in the given pressure domain. Over this region it can be assumed that the zirconolite material adopts a more symmetric structure, most likely within nanocrystalline domains where some of the original complex monoclinic features are maintained. We observed a similar phenomenon in the $Bi_2Ti_2O_7$ system,

which undergoes a transformation above 33 GPa to a disordered fluorite-like structure with broad features.[22] We believe some level of similarity is becoming evident in the structural evolution of pyrochlore-like systems as a function of pressure. The energetic pathway seems to be towards the formation of a disordered phase at the higher pressure limits and that is what causes metastability and the repeating claims of amorphous-like behaviour.

Our structural analysis of the recovered phase suggests that at the highest pressures zirconolite forms either a defective fluorite structure or a disordered cottunite-type structure. In the case of the fluorite like models, the presence of a distortion that is not observed in the defective fluorite material derived from $Bi_2Ti_2O_7$ under pressure, may be linked to the compression along the [111] axis of the parent fluorite structure which is already present in the zirconolite structure. The need to include a rhombohedral distortion in order to fit the peak positions at high pressure would suggest that the cation positions have not been fully disordered during the compression process. In the cotunnite case the cation positions could be more fully disordered and it is possible to envisage this occurring during the phase transition from the fluorite-like lattice that is present in the original zirconolite structure and presumably in the intermediate pressure crystalline phase. Further investigations will be required to finally discern which of these structure models is most correct.

Conclusions

The high pressure structural behavior of zirconolite ($CaZrTi_2O_7$) at geologically relevant pressures has been investigated for the first time. The combination of using both synchrotron X-ray diffraction techniques and Raman spectroscopy has led to the observation of two high pressure phases and a developing link in understanding the behaviour of similar pyrochlore-like systems at high pressure and ambient temperature. With quasi-hydrostatic loadings in He the onset of an intermediate phase is observed via a first order pathway at 15.6 GPa identified with indistinguishable $P\,2_1$ or $P\,2_1/m$ symmetry. No complete structural solution was identified for this phase partly due to difficulties arising from a long pressure co-existence with that of the ambient structure for over 20 GPa. Above 56 GPa the transformation into a disordered phase is observed that persists up to a maximum measured pressure of 80 GPa. Our Raman studies initially suggested the possibility of pressure induced amorphization, however synchrotron X-ray data confirm the crystalline but highly disordered nature of this high pressure phase. Due to the strong disordering present in this phase and consequently the broad data a single structural model could not be confirmed and therefore we suggest that the two most likely structural candidates identified are either a defective fluorite structure or a disordered cottunite-type structure. A key feature of this disordered high pressure phase is that it is fully recoverable to ambient pressure and demands further investigation.

Acknowledgements

The authors would like to thank Scott Owens, Ewan Mandrell and Henry Foxhall for valuable discussions. AS and GG acknowledge the European Synchrotron Radiation Facility for provision of synchrotron radiation facilities. PFM was funded by EPSRC Senior Research Fellowship EP/D07357X; NCH and MCS are grateful to EPSRC for funding under Grant EP/F055412/1; NCH is also grateful to the Royal Academy of Engineering and the Nuclear Decommissioning Authority for funding support.

References

1. Ringwood, A. E.; Kesson, S. E.; Ware, N. G.; Hibberson, W.; Major, A., *Nature* **1979,** 278, 219.
2. Sinclair, W.; Ringwood, A. E., *Geochem. J.* **1981,** 15, 229.
3. Gatehouse, B. M.; Grey, I. E.; Hill, R. J.; Rossell, H. J., *Acta Crystallographica Section B* **1981,** 37, 306.
4. White, T. J., *American Mineralogist* **1984,** 69, 1156.
5. Coelho, A. A.; Cheary, R. W.; Smith, K. L., *Journal of Solid State Chemistry* **1997,** 129, 346.
6. Grey, I. E.; Mumme, W. G.; Ness, T. J.; Roth, R. S.; Smith, K. L., *Journal of Solid State Chemistry* **2003,** 174, 285.
7. Whittle, K. R.; Hyatt, N. C.; Smith, K. L.; Margiolaki, I.; Berry, F. J.; Knight, K. S.; Lumpkin, G. R., *American Mineralogist* **2012,** 97, 291.
8. Lumpkin, G. R., *Journal of Nuclear Materials* **2001,** 289, 136.
9. Lumpkin, G. R.; Hart, K. P.; McGlinn, P. J.; Payne, T. E.; Giere, R.; Williams, C. T., *Radiochimica Acta* **1994,** 66-7, 469.
10. Reid, D. P.; Hyatt, N. C.; Stennett, M. C.; Maddrell, E. R., *Materials World* **2011,** 19, 26.
11. Caurant, D.; Loiseau, P.; Bardez, I., *Journal of Nuclear Materials* **2010,** 407, 88.
12. Gilbert, M. R.; Selfslag, C.; Walter, M.; Stennett, M. C.; Somers, J.; Hyatt, N. C.; Livens, F. R., *IOP Conference Series: Materials Science and Engineering* **2007,** 9, 012007.
13. Strachan, D. M.; Scheele, R. D.; Buck, E. C.; Kozelisky, A. E.; Sell, R. L.; Elovich, R. J.; Buchmiller, W. C., *Journal of Nuclear Materials* **2008,** 372, 16.
14. Lumpkin, G. R., *Elements* **2006,** 2, 365.
15. Begg, B. D.; Vance, E. R.; Conradson, S. D., *Journal of Alloys and Compounds* **1998,** 271, 221.
16. Weber, W. J.; Ewing, R. C.; Catlow, C. R. A.; de la Rubia, T. D.; Hobbs, L. W.; Kinoshita, C.; Matzke, H.; Motta, A. T.; Nastasi, M.; Salje, E. K. H.; Vance, E. R.; Zinkle, S. J., *Journal of Materials Research* **1998,** 13, 1434.
17. Farges, F.; Ewing, R. C.; Brown, G. E., *Journal of Materials Research* **1993,** 8, 1983.
18. Reid, D. P.; Stennett, M. C.; Ravel, B.; Woicik, J. C.; Peng, N.; Maddrell, E. R.; Hyatt, N. C., *Nuclear Instruments and Methods in Physics Research Section B: Beam Interactions with Materials and Atoms* **2010,** 166-167, 293.
19. Hemley, R. J.; Jephcoat, A. P.; Mao, H. K.; Ming, L. C.; Manghnani, M. H., *Nature* **1988,** 334, 52.
20. Wentzcovitch, R. M.; da Silva, C.; Chelikowsky, J. R.; Binggeli, N., *Physical Review Letters* **1998,** 80, 2149.

21. Cabrera, R. Q.; Salamat, A.; Barkalov, O. I.; Leynaud, O.; Hutchins, P.; Daisenberger, D.; Machon, D.; Sella, A.; Lewis, D. W.; McMillan, P. F., *Journal of Solid State Chemistry* **2009,** 182, 2535.

22. Salamat, A.; Hector, A. L.; McMillan, P. F.; Ritter, C., *Inorganic Chemistry* **2011,** 50, 11905.

23. Dewaele, A.; Loubeyre, P.; Mezouar, M., *Physical Review B* **2004,** 70, 8.

24. Soignard, E.; McMillan, P., *Chemistry of Materials* **2004,** 16, 3533.

25. Hammersley, A. P.; Svensson, S. O.; Hanfland, M.; Fitch, A. N.; Hausermann, D., *High Pressure Research* **1996,** 14, 235.

26. Larson, A. C.; Dreele, R. B. V., *Los Alamos National Laboratory Report LAUR 86-748* **2000**.

27. Toby, B. H., *Journal of Applied Crystallography* **2001,** 34, 210.

28. Barkalov, O. I.; Tissen, V. G.; McMillan, P. F.; Wilson, M.; Sella, A.; Nefedova, M. V., *Physical Review B* **2010,** 82, 4.

29. Paul, F. M. a. M. W. a. M. C. W., *Journal of Physics: Condensed Matter* **2003,** 15, 6105.

30. Swamy, V.; Kuznetsov, A.; Dubrovinsky, L. S.; McMillan, P. F.; Prakapenka, V. B.; Shen, G.; Muddle, B. C., *Physical Review Letters* **2006,** 96, 4.

31. Spengler, W.; Kaiser, R., *Solid State Communications* **1975,** 17, 19.

32. Spengler, W.; Kaiser, R., *Solid State Communications* **1976,** 18, 881.

33. Spengler, W.; Kaiser, R.; Christensen, A. N.; Vogt, G. M., *Phys. Rev. B* **1978,** 17, 1095.

34. Guo, H. Z.; Chen, Z. H.; Cheng, B. L.; Lu, H. B.; Liu, L. F.; Zhou, Y. L., *Journal of the European Ceramic Society* **2005,** 25, 2347.

35. Grzechnik, A.; Wolf, G. H.; McMillan, P. F., *Journal of Raman Spectroscopy* **1997,** 28,, 885.

36. Henderson, S. J.; Shebanova, O.; Hector, A. L.; McMillan, P. F.; Weller, M. T., *Chemistry of Materials* **2007,** 19, 1712.

37. Birch, F., *Physical Review* **1947,** 71, 809.

38. Birch, F., *J. Geophys. Res* **1978,** 83, 1257.

39. Jeanloz, R., *Geophys. Res. Lett.* **1981,** 88, 1219.

40. Syono, Y.; Manghnani, M. H., *Terra Scientific Publishing Company* **1992,** Mineral Physics Vol 3.

41. Duffy, T. S.; Wang, Y., *Ultrahigh-Pressure Mineralogy* **1998,** 37, (425).

42. Zhang, F. X.; Manoun, B.; Saxena, S. K.; Zha, C. S., *Applied Physics Letters* **2005,** 86, (18), 181906.

43. Hahn, T., *International Tables for Crystallography: Volume A, Kluwer Academic Publishers, Dordrecht* **2002**.

44. Lee, J.-H.; Chiang, Y.-M., *Journal of Electroceramics* **2001,** 6, (1), 7.

45. Zhang, F. X.; Lang, M.; Becker, U.; Ewing, R. C.; Lian, J., *Applied Physics Letters* **2008,** 92, 011909.

46. Goel, P.; Choudhury, N.; Chaplot, S. L., *Journal of Physics: Condensed Matter* **2007,** 19, 386239.

47. Jayaraman, A.; Kourouklis, G.; van Uitert, L., *Pramana* **1988,** 30, 225.

48. Desgreniers, S.; Lagarec, K., *Physical Review B* **1999,** 59, 8467.

49. Zhang, F. X.; Manoun, B.; Saxena, S. K.; Zha, C. S., *Applied Physics Letters* **2005,** 86, 181906.

50. Zhang, F. X.; Saxena, S. K., *Chemical Physics Letters* **2005,** 413, 248.